Energy & Environmental Science

ROYAL SOCIETY OF CHEMISTRY

PAPER

View Article Online
View Journal | View Issue

Cite this: *Energy Environ. Sci.*, 2024, **17**, 6616

High-solvation electrolytes for ultra-stable calcium-ion storage†

Junjun Wang,‡[ab] Ruohan Yu,‡[a] Yalong Jiang,[a] Fan Qiao,[a] Xiaobin Liao,[a] Jianxiang Wang,[a] Meng Huang,[a] Fangyu Xiong,[a] Lianmeng Cui,[a] Yuhang Dai,[a] Lei Zhang,[a] Qinyou An,*[ac] Guanjie He*[b] and Liqiang Mai*[ac]

Received 8th May 2024,
Accepted 29th July 2024

DOI: 10.1039/d4ee02003k

rsc.li/ees

Calcium-ion batteries (CIBs) have potential as electrochemical energy storage devices due to the low redox potential of Ca^{2+}/Ca and the abundant reserves of Ca. However, the unsatisfactory calcium storage performance of electrode materials limits the development of CIBs. Here, we propose a design principle of high-solvation electrolytes to achieve ultra-stable calcium-ion storage. In high-solvation electrolytes, the decomposition of $TFSI^-$ ions and the formation of a CaF_2-rich cathode electrolyte interface with Ca^{2+} insulation can be suppressed. With this electrolyte, $Na_2V_6O_{16}{\cdot}2.9H_2O$ shows a high discharge capacity of 240.7 mA h g^{-1} at 20 mA g^{-1} and an ultra-long life of 60 000 cycles (over 600 days) at 1000 mA g^{-1}. A three-dimensionally reduced graphene oxide aerogel and $(NH_4)_2V_6O_{16}{\cdot}1.5H_2O$ also exhibit a long life of 6000 cycles and 9000 cycles, respectively. These materials have the longest cycle life among reported materials so far in CIBs. This work endows the electrode materials with ultra-stable calcium-ion storage and provides a design principle of electrolytes for cathode materials in CIBs.

Broader context

The reserves of raw materials play a crucial role in whether electrochemical energy storage devices can be used for large-scale energy storage. Due to the low redox potential of Ca^{2+}/Ca (−2.87 V *vs.* SHE close to that of Li^+/Li) and the abundant reserves of Ca in the earth's crust, Ca-ion batteries (CIBs) have received widespread attention from researchers as potential electrochemical energy storage devices. However, the unsatisfactory Ca storage performance of electrode materials limits the development of CIBs. In this work, we studied for the first time the correlation between the solvation structure of electrolytes and the performance of cathode materials in CIBs. The results indicated that the decomposition of $TFSI^-$ ions and the formation of the CaF_2-rich cathode electrolyte interface with Ca^{2+} insulation can be suppressed in a high-solvation Ca electrolyte. Finally, we proposed a design principle of Ca electrolytes for cathode materials with ultra-stable calcium-ion storage.

Introduction

The low reserves of raw materials (such as Li, Ni, and Co) for lithium-ion batteries (LIBs) make them unsuitable for large-scale energy storage, which motivates researchers to develop new electrochemical energy storage systems based on abundant materials, such as sodium-ion, potassium-ion, multivalent-ion batteries, *etc.* Since each multivalent-ion can transfer two or three electrons, multivalent-ion batteries are expected to be energy storage devices with higher energy density and lower cost.[1–3] In addition, compared with Li, Na or K metal anodes, Mg and Ca metal anodes are less likely to form dendrites, which can effectively improve the safety of batteries.[4] Therefore, multivalent-ion batteries are considered potential candidates for post-LIBs.

Among multivalent-ion (Al^{3+}, Zn^{2+}, Mg^{2+}, and Ca^{2+}) batteries, Ca^{2+}/Ca has the lowest redox potential of −2.87 V *vs.* standard hydrogen electrode (SHE), which is close to that of Li^+/Li (−3.04 V *vs.* SHE). Therefore, calcium-ion batteries (CIBs) can achieve higher working voltage and energy density among these multivalent-ion batteries. In addition, Ca^{2+} has the lowest

[a] *State Key Laboratory of Advanced Technology for Materials Synthesis and Processing, Wuhan University of Technology, Wuhan 430070, China. E-mail: mlq518@whut.edu.cn, anqinyou86@whut.edu.cn*
[b] *Christopher Ingold Laboratory, Department of Chemistry, University College London, 20 Gordon Street, London, WC1H 0AJ, UK. E-mail: g.he@ucl.ac.uk*
[c] *Hubei Longzhong Laboratory, Wuhan University of Technology (Xiangyang Demonstration Zone), Xiangyang 441000, Hubei, China*

† Electronic supplementary information (ESI) available. See DOI: https://doi.org/10.1039/d4ee02003k

‡ These authors contributed equally to this work.

charge density, Ca metal tends to be uniformly deposited/stripped, and Ca is the fifth most abundant element, meaning that CIBs have good rate performance, low cost, and high safety. However, the unsatisfactory calcium storage performance of electrode materials, caused by the large radius and divalent nature of Ca^{2+} and the decomposition of electrolytes, limits the development of CIBs. In the past two decades, considerable efforts have been made to develop electrolytes compatible with Ca metal anodes, and some breakthroughs have been made, such as $Ca(BF_4)_2$/ethylene carbonate:propylene carbonate,[5] $Ca(BH_4)_2$/tetrahydrofuran[6] and $Ca[B(hfip)_4]_2$/glyme (DME).[7] Recently, Zhang *et al.* realized the compatibility of $Ca(TFSI)_2$-based electrolytes with the Ca metal anode by regulating the solvation structure of Ca^{2+}.[8] Unfortunately, these electrolytes are poorly compatible with cathode materials. $Ca(TFSI)_2$, as a commercially available and highly compatible salt, has been used in ~50% of the reported cathode materials for CIBs. However, most electrode materials exhibited poor cycling performance or low specific capacity (Table S1, ESI†). The electrolyte solvation structure has been shown to have significant impacts on the cathode materials' performance in monovalent ion (Li^+/Na^+/K^+) and multivalent-ion (Mg^{2+}/Zn^{2+}) batteries.[3,9–12] However, the correlation between the solvation structure of electrolytes and the performance of cathode materials in CIBs is unclear. Therefore, it is of great significance to study the correlations between the solvation structure of Ca^{2+} and the cathode materials' performance in $Ca(TFSI)_2$-based electrolytes and propose a design principle of Ca electrolytes for ultra-stable calcium-ion storage.

Here, we regulate the solvation structure of Ca^{2+} in $Ca(TFSI)_2$-based electrolytes by using different solvation power solvents, including DME, diglyme (G2), and tetraglyme (G4). Classical molecular dynamics (CMD) simulation and Raman spectrum data indicate that the solvation degree of Ca^{2+} increases with the solvent from DME to G2 and G4. With a high-solvation and well-compatible $Ca(TFSI)_2$/G4 electrolyte, $Na_2V_6O_{16}\cdot 2.9H_2O$ (NVO) shows an ultra-long life of 20 000 cycles at room temperature and 60 000 cycles (over 600 days) at 50 °C. A three-dimensional reduced graphene oxide (3D rGO) aerogel and $(NH_4)_2V_6O_{16}\cdot 1.5H_2O$ (NHVO) also exhibit a long life of 6000 and 9000 cycles, respectively. The formation and composition of the cathode electrolyte interphase (CEI) in CIBs were first studied by *ex situ* transmission electron microscopy (TEM) and X-ray photoelectron spectroscopy (XPS). The results demonstrate that the excellent cycling performance of the electrode materials benefits from minimizing the decomposition of the $TFSI^-$ ion and preventing the formation of the CaF_2-rich CEI in the high-solvation $Ca(TFSI)_2$/G4 electrolyte. In addition, taking NVO as a representative, the differences in the calcium storage mechanism and electrolyte kinetic behavior in different solvation electrolytes were studied through *in situ* X-ray diffraction (XRD), *in situ* attenuated total reflectance Fourier-transform infrared (ATR-FTIR), and 3D tomography reconstruction technologies. And, the crystal structure and Ca^{2+} storage site of NVO were observed for the first time at the atomic scale by double aberration correction TEM.

Results and discussion

Calcium electrolyte design principles

The design principles of $Ca(TFSI)_2$-based electrolytes are summarized in Fig. 1a–c. In low-solvation electrolytes (Fig. 1a), the primary solvation sheath of Ca^{2+} contains $TFSI^-$ ions, and the $TFSI^-$ ions are reduced during the discharge process,[10] leading to CaF_2-rich CEI formation and electrolyte consumption. In addition, CaF_2 is unfavorable for the conduction of Ca^{2+}.[13] Therefore, electrode materials may exhibit poor cycling performance in low-solvation electrolytes due to the continuous consumption of electrolytes and the formation of the CaF_2-rich CEI. In high-solvation electrolytes (Fig. 1b), the $TFSI^-$ ions exist as solvent-separated ion pairs (SSIPs) or free ions. The $TFSI^-$ ions do not exist in the primary solvation sheath of Ca^{2+} and do not migrate to the cathode side during discharge. As a result, the reduction of $TFSI^-$ ions at the electrode interface is minimized during the discharge process, which prevents the formation of the CaF_2-rich CEI and the consumption of electrolyte, further enhancing the cycling performance of electrode materials. As shown in Fig. 1c, the proposed design principle of $Ca(TFSI)_2$-based electrolytes is to inhibit the reduction of $TFSI^-$ by utilizing high-solvating power solvents.

To illustrate the correlation between solvents with different solvating powers and the solvation structure of Ca^{2+} in $Ca(TFSI)_2$-based electrolytes, three ether solvents with different chain lengths (DME, G2, and G4) are considered. Gaussian calculated electrostatic potentials (φ) of different solvents and the corresponding binding energies between Ca^{2+} and solvents are shown in Fig. 1d–f and Fig. S1 (ESI†). The results indicate that the solvent molecules show high negative charge densities near oxygen atoms, and these oxygen atoms may coordinate with Ca^{2+} in electrolytes. The binding energies between Ca^{2+} and solvent oxygen atoms increase with solvent from DME, G2 to G4, and the minimum formation energies are −3.97, −4.52, and −5.6 eV, respectively. The results indicate that G4 has a higher solvating power. CMD simulations were performed to study the solvation structure and the coordinated numbers (CNs) of Ca^{2+} in $Ca(TFSI)_2$/DME, $Ca(TFSI)_2$/G2 and $Ca(TFSI)_2$/G4 electrolytes (Fig. 1g–j and Fig. S2 and S3, ESI†). The results (Fig. 1g–i and Fig. S2, ESI†) illustrate that the primary solvation sheath of Ca^{2+} in $Ca(TFSI)_2$/G4 does not contain $TFSI^-$. In addition, we calculated the CNs of Ca^{2+} in different electrolytes (Fig. 1j) based on the radial distribution functions (RDF) (Fig. S3, ESI†). The CNs of $TFSI^-$ decrease as the solvent changed from DME, G2 to G4. Almost no $TFSI^-$ are present in the primary solvation sheath of Ca^{2+} in $Ca(TFSI)_2$/G4, indicating that $Ca(TFSI)_2$/G4 is a high-solvation electrolyte. Raman spectra (Fig. 1k) of different electrolytes are used to analyze $TFSI^-$–Ca^{2+} interactions due to the $TFSI^-$ complex breathing mode located at 735–755 cm^{-1} and the 740 cm^{-1} mode corresponding to SSIPs or free $TFSI^-$ ions (without Ca^{2+} coordination).[8,14,15] The results suggest that almost no $TFSI^-$–Ca^{2+} interactions are found in $Ca(TSFI)_2$/G4, which is well consistent with the results of CMD simulations. The Fourier transform infrared (FTIR) spectra of different electrolytes are shown in Fig. S4 (ESI†). The vibrational

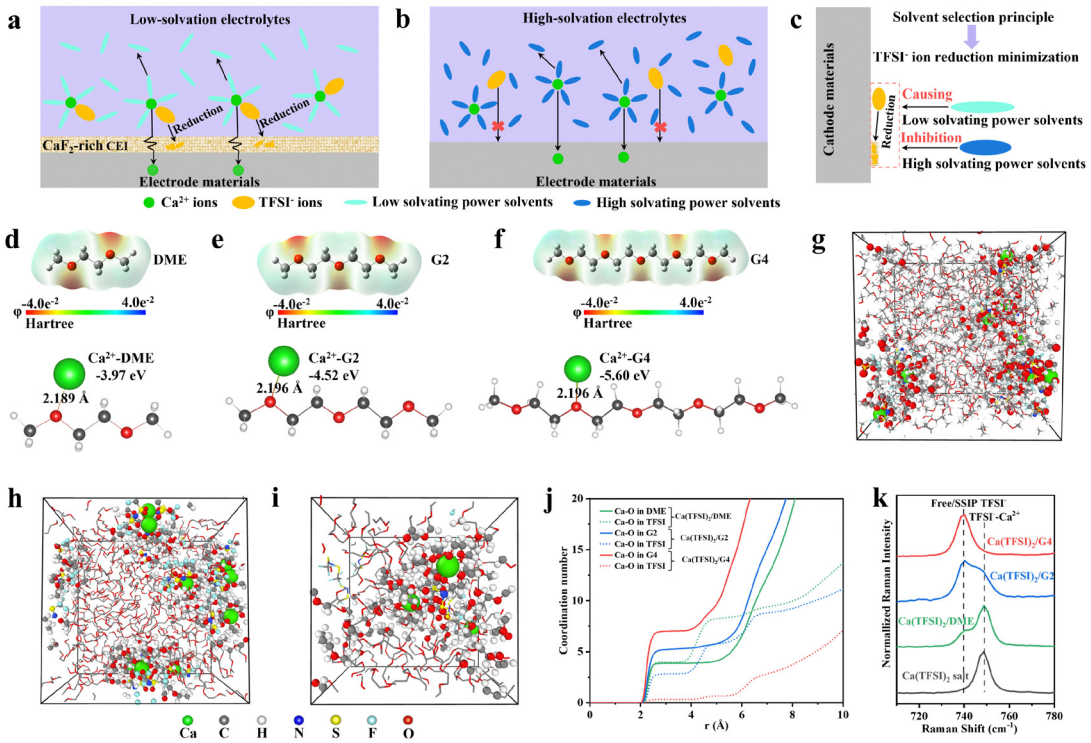

Fig. 1 Design principles and physicochemical characterization of $Ca(TFSI)_2$-based electrolytes. (a) In the low-solvation electrolytes, the reduction of $TFSI^-$ ions leads to constant consumption of electrolytes and the formation of CaF_2-rich CEI on the electrode surface. (b) In the high-solvation electrolytes, the reduction of $TFSI^-$ ions is inhibited. (c) The design principle of $Ca(TFSI)_2$-based electrolyte is to minimize the reduction of $TFSI^-$ ions: select high solvating power solvents to increase the solvation degree of electrolytes. (d)–(f) Gaussian calculated electrostatic potentials (φ) of different solvents and the corresponding binding energies between Ca^{2+} and the solvent: (d) DME, (e) G2, and (f) G4. (g)–(i) CMD simulation of $Ca(TFSI)_2$-based electrolytes: snapshots of CMD simulations of 0.3 M $Ca(TFSI)_2$ in (g) DME, (h) G2 and (i) G4. (j) The coordination numbers of Ca^{2+} in different electrolytes. (k) Raman spectra of $Ca(TFSI)_2$ salt and $Ca(TFSI)_2$ in different solvents.

features in the range of 1300–1400 cm^{-1} correspond to the asymmetric $-SO_2$ stretching bands in $TFSI^-$ ions, which are usually used to observe ion–ion interactions.[16–18] In the $Ca(TFSI)_2$/G4 electrolyte, the peak shape of the asymmetric $-SO_2$ stretching bands is consistent with the vibrational peaks of free $TFSI^-$ ions in $Zn(TFSI)_2$ and LiTFSI,[17,18] indicating the presence of only free $TFSI^-$ ions in the $Ca(TFSI)_2$/G4 electrolyte. The analysis of the FTIR spectra further confirms the results of the Raman spectra. Cu// activated carbon cloth (ACC) batteries with different electrolytes were assembled to illustrate the effects of solvent molecules on the decomposition of $TFSI^-$. Cyclic voltammetry (CV) curves of Cu// ACC at 0.1 mV s^{-1} are shown in Fig. S5 (ESI†). In $Ca(TFSI)_2$/DME and $Ca(TFSI)_2$/G2, the reduction peaks are observed in the range from −0.8 to −0.5 V *vs.* ACC, corresponding to the decomposition of $TFSI^-$.[8] Interestingly, the reduction peak is absent in $Ca(TFSI)_2$/G4. The result indicates that the decomposition of $TFSI^-$ can be effectively inhibited in the $Ca(TFSI)_2$/G4 electrolyte. In addition, the results of linear sweep voltammetry (LSV) demonstrate that the $Ca(TFSI)_2$/G4 electrolyte has high oxidation stability (Fig. S6, ESI†).

Calcium storage performance in high-solvation electrolytes

The above results demonstrate that $TFSI^-$ is reduced in low-solvation electrolytes during discharge. However, further verification is needed to determine whether the reduction of $TFSI^-$ will affect the performance of electrode materials. NVO with large layer spacing and Na^+ pillars was synthesized by hydrothermal method (Fig. S7, ESI†) and used as a cathode material to study the effect of the solvation structure of Ca^{2+} on the Ca^{2+} storage performance. The XRD pattern of NVO (Fig. 2a) can be well indexed to the PDF card of $Na_2V_6O_{16}{\cdot}3H_2O$ (PDF#: 00-016-0601), and the scanning electron microscopy (SEM) image shows that NVO is ultra-long nanowires (Fig. S8, ESI†). The high magnification high-angle annular dark-filed (HAADF) scanning transmission electron microscopy (STEM) images of NVO are shown in Fig. 2b and c and Fig. S9 (ESI†). The crystal structure of NVO was observed for the first time at the atomic scale. The bright dots in the HAADF-STEM images are assigned to heavy V atoms, and the position of the V atoms is consistent with the crystal structure of NVO along *a* and *b* directions (Fig. 2b and Fig. S9, ESI†). The HAADF-STEM image of NVO further indicates that NVO is a layered structure material with a large layer spacing of 0.79 nm, corresponding to the (001) crystal plane of NVO (Fig. 2c). Some other characterization techniques for NVO are shown in Fig. S10–S12 (ESI†). The results indicate that the valence state of V in NVO is +5 and each NVO contains 2.9 H_2O molecules.

Since the $Ca(TFSI)_2$/DME electrolyte is not compatible with the Ca metal,[14] ACC is selected as the counter electrode with a

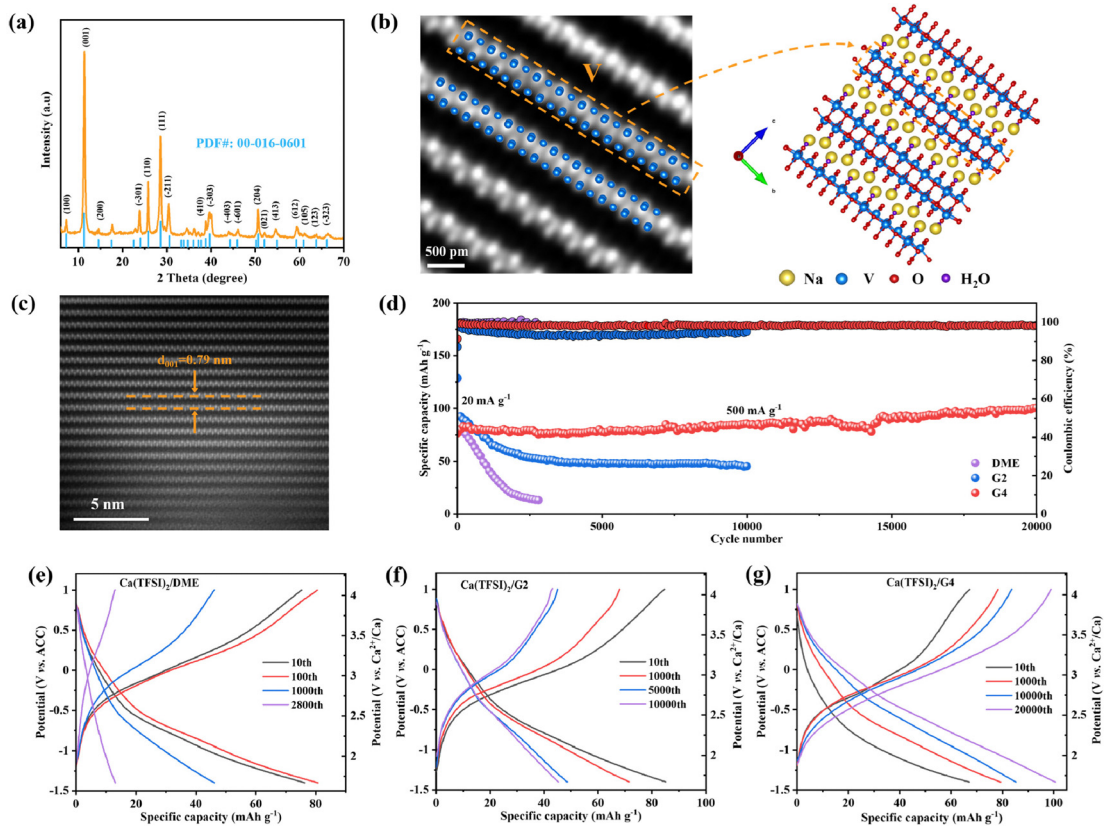

Fig. 2 Calcium storage performance of $Na_2V_6O_{16}{\cdot}2.9H_2O$ in different electrolytes. (a) XRD pattern of NVO. (b) and (c) HAADF-STEM images of NVO and corresponding crystal structures along *a* direction. (d) Cycling performance of NVO with different electrolytes at 500 mA g^{-1} and room temperature after five cycles at 20 mA g^{-1} (the loading of the active material is ~1.1 mg cm^{-2}). (e)–(g) Charge/discharge profiles as a function of cycle number of NVO using (e) Ca(TFSI)$_2$/DME, (f) Ca(TFSI)$_2$/G2, and (g) Ca(TFSI)$_2$/G4 electrolytes.

stable potential of 3.068 V *vs.* Ca^{2+}/Ca (Fig. S13, ESI†).[19] The Ca^{2+} storage performance of NVO in three different electrolytes was characterized at room temperature (Fig. 2d). The cell with Ca(TFSI)$_2$/DME shows poor cycling performance, including rapid capacity fading by 84.0% after 2800 cycles and increased cell overpotential during cycling (Fig. 2e). The cell in the Ca(TFSI)$_2$/G2 electrolyte exhibits improved cycling performance, but capacity fading and increased cell overpotential are still observed (Fig. 2f). The capacity retention of NVO is 48.5% after 10 000 cycles in the Ca(TFSI)$_2$/G2 electrolyte. In contrast, the cell with a high-solvation Ca(TFSI)$_2$/G4 electrolyte shows a long-life of 20 000 cycles and the capacity increases gradually. The overpotential of the cell gradually decreases during 20 000 cycles as shown in Fig. 2g with a high Coulombic efficiency (CE). In addition, in the Ca(TFSI)$_2$/G4 electrolyte, NVO can also exhibit a high discharge capacity of 240 mA h g^{-1} and excellent cycling performance at low current density (Fig. S14, ESI†). The high calcium storage capacity of NVO has also been verified in a three-electrode system (Fig. S15, ESI†). The reasons for the capacity increase and overpotential decrease during the cycle will be discussed in detail later. Combining the CMD simulation, Raman spectroscopy and FTIR spectroscopy analysis results of electrolytes, the electrochemical performance testing indicates that electrolytes with a high proportion of SSIPs or free $TFSI^-$ ions are conducive to achieving long cycling lifetimes of electrode materials.

Cathode electrolyte interface components in different solvation electrolytes

The above electrochemical performance tests have shown that NVO has the best cycling performance in high-solvation Ca(TFSI)$_2$/G4 electrolyte, whether this is related to suppressed reduction of $TFSI^-$ ions needs to be further studied. The composition and properties of the CEI layer on the cycled NVO electrode surface with different electrolytes were analyzed by XPS and TEM. In low-solvation Ca(TFSI)$_2$/DME and Ca(TFSI)$_2$/G2, the reduction of $TFSI^-$ induces the formation of inorganic-rich CEI, including CaF_2 and S-based compounds (Fig. 3a and b and Fig. S16a and b, ESI†). In sharp contrast, in high-solvation Ca(TFSI)$_2$/G4, the peak corresponding to CaF_2 is very weak even after 210 s Ar^+ sputtering (Fig. 3c) and the sulfur-based compounds are not observed (Fig. S16c, ESI†), which indicates that the decomposition of $TFSI^-$ ions can be significantly suppressed in a high-solvation electrolyte.

The STEM image for the cycled NVO electrode in Ca(TFSI)$_2$/DME (Fig. 3d and Fig. S17, ESI†) demonstrates the presence of a 2.3 nm thick CEI on the surface of NVO. The HAADF-STEM image and elemental maps show that the edge of NVO contains

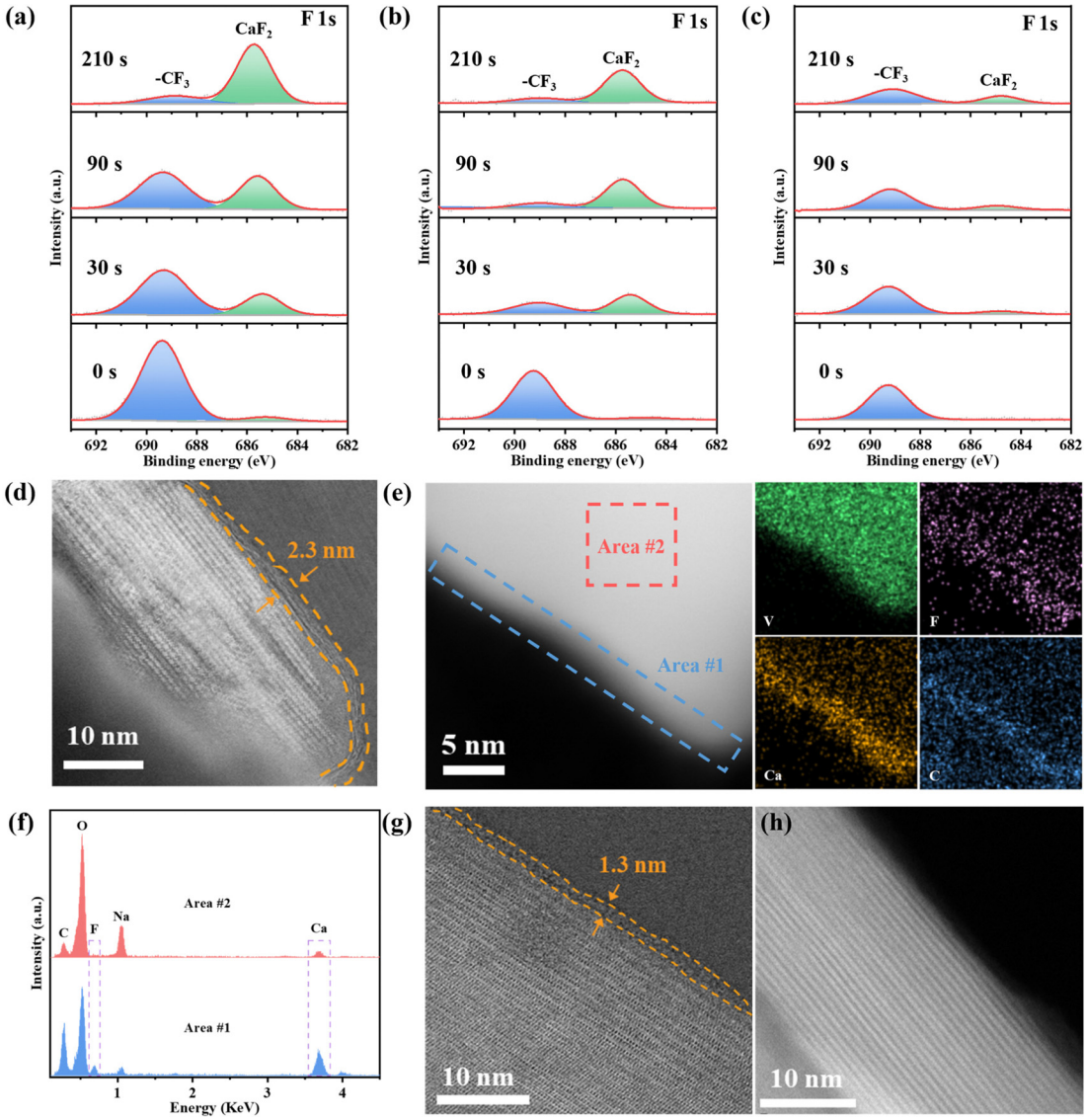

Fig. 3 Characterization of the cathode electrolyte interface components. (a)–(c) F 1s XPS spectra of the cycled NVO with different sputtering times in (a) $Ca(TFSI)_2$/DME, (b) $Ca(TFSI)_2$/G2, and (c) $Ca(TFSI)_2$/G4 electrolytes. (d) STEM image and (e) HAADF-STEM image with corresponding elemental maps of the cycled NVO in $Ca(TFSI)_2$/DME. (f) EDX spectra corresponding to the selected area in (e). (g) and (h) STEM image of the cycled NVO in (g) $Ca(TFSI)_2$/G2 and (h) $Ca(TFSI)_2$/G4.

more F, Ca, and C elements (Fig. 3e). The EDX spectra (Fig. 3f) additionally indicate the formation of CaF_2-rich CEI in $Ca(TFSI)_2$/DME. The cycled NVO STEM image in $Ca(TFSI)_2$/G2 shows a thinner CEI of 1.3 nm (Fig. 3g). In contrast, in high-solvation $Ca(TFSI)_2$/G4 electrolyte, almost no CEI can be observed on the surface of NVO, which also confirms that the decomposition of $TFSI^-$ and the formation of CaF_2-rich CEI can be suppressed in the $Ca(TFSI)_2$/G4 electrolyte. In addition, the stable NVO in these electrolytes verifies that the fading of capacity in the low solvation-electrolytes is not caused by the loss of active material (Fig. S18, ESI†). XPS and TEM results show that the cycling performance of NVO is closely related to the solvation structure of Ca^{2+} and the inhibition of $TFSI^-$ decomposition is beneficial for electrode materials to achieve stable calcium-ion storage.

High-temperature performance and compatibility of high-solvation electrolytes

To demonstrate the high-temperature performance and compatibility of the $Ca(TFSI)_2$/G4 electrolyte, the calcium storage performances of NVO and NHVO at 50 °C and the 3D rGO aerogel at room temperature were evaluated. NVO shows a high discharge capacity of 210.7 mA h g^{-1} without capacity fading after 100 cycles at 100 mA g^{-1} (Fig. 4a and Fig. S19, ESI†) and exhibits a capacity of 148.0 mA h g^{-1} at 1000 mA g^{-1} (Fig. S20, ESI†). It is impressing that NVO can maintain a capacity of 110.9 mA h g^{-1} with a capacity retention of 75% after 60 000 cycles (over 600 days, Fig. 4b). To the best of our knowledge, the 60 000 cycles in CIBs are the longest. In addition, when the test temperature turns from 50 °C to 25 °C and back to 50 °C, NVO can still maintain stable cycling performance. Rate performance

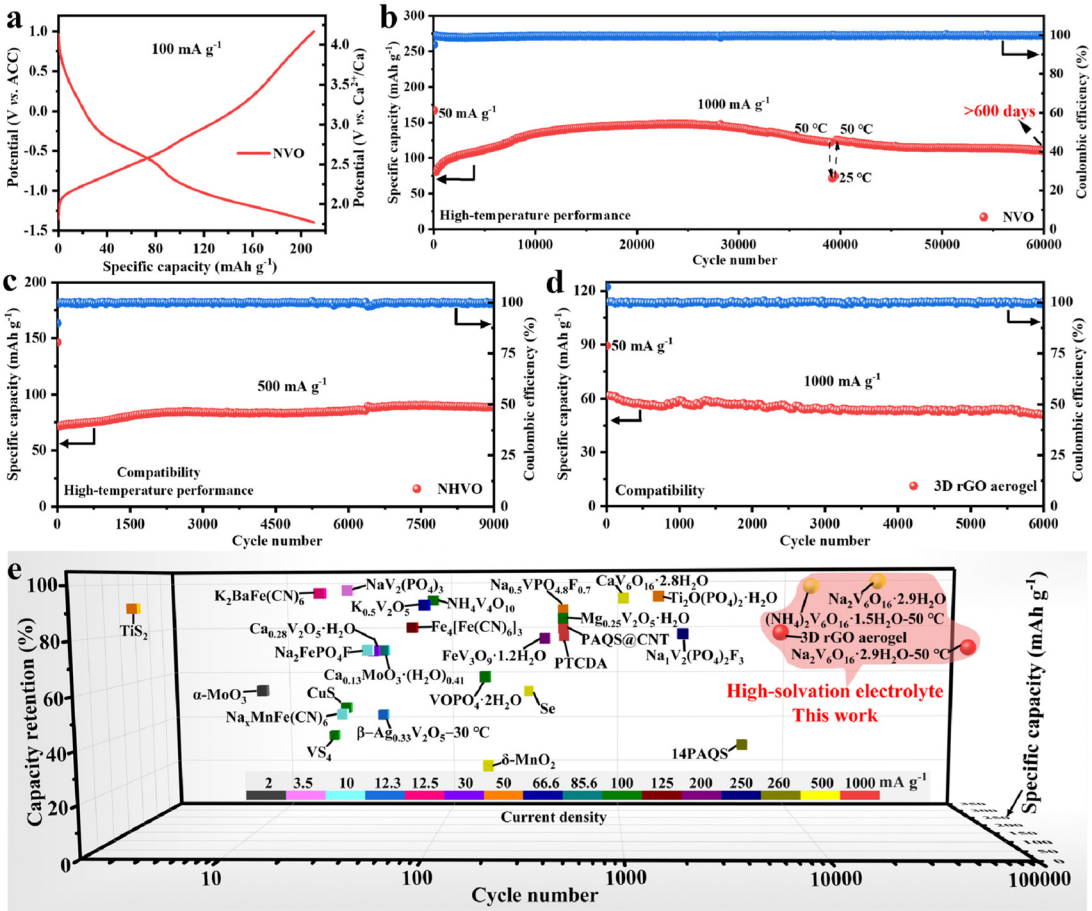

Fig. 4 High-temperature performance and compatibility of high-solvation electrolytes. (a) Galvanostatic charge/discharge profiles of NVO at 100 mA g^{-1} and 50 °C. (b)–(d) Cycling performances of (b) NVO at 1000 mA g^{-1} and 50 °C, (c) NHVO at 500 mA g^{-1} and 50 °C and (d) 3D rGO aerogel at 1000 mA g^{-1}. (e) Comparison of the Ca^{2+} storage performance of the 3D rGO aerogel, NHVO, and NVO with reported cathode materials for CIBs in organic electrolyte.[20–45]

tests show that NVO has a capacity of 59.1 mA h g^{-1} at 3000 mA g^{-1} (Fig. S21, ESI†). The effects of interlayer H_2O on the calcium storage performance and the reaction kinetics in $Ca(TFSI)_2$/G4 are additionally investigated (Fig. S22–S23, ESI†). The results demonstrate that the interlayer H_2O molecules play an important role in achieving excellent calcium storage performance, and the average diffusion rate Ca^{2+} in the NVO electrode is 2.8×10^{-11} cm^2 s^{-1}.

In addition, NHVO exhibits a capacity of 71 mA h g^{-1} and a long-life of 9000 cycles at 500 mA g^{-1} (Fig. 4c and Fig. S24, ESI†). The 3D rGO aerogel delivers a capacity of 62 mA h g^{-1} and 6000 cycles with 81.5% capacity retention at 1000 mA g^{-1} (Fig. 4d and Fig. S25, ESI†). The results indicate that NHVO and 3D rGO aerogel can also exhibit excellent cycling stability in $Ca(TFSI)_2$/G4, meaning that $Ca(TFSI)_2$/G4 has good compatibility with electrode materials. To assess the compatibility of the high-solvation $Ca(TFSI)_2$/G4 electrolyte with the Ca metal anode, the performance of NVO‖Ca and Ca‖Ca cells in the $Ca(TFSI)_2$/G4 electrolyte was evaluated. The observed poor electrochemical performance suggests that the $Ca(TFSI)_2$/G4 electrolyte is not compatible with the Ca metal anode (Fig. S26, ESI†). XPS depth profile analysis indicates that the SEI on the surface of the cycled Ca metal anode contains CaF_2 and CaO (Fig. S27, ESI†), which have been shown to have high diffusion barriers for Ca^{2+} ions.[46] The poor compatibility could be attributed to the particularly strong and well-defined G4:Ca^{2+} interactions.[14,47] Finally, the electrochemical performances of 3D rGO aerogel, NHVO, and NVO are compared with the reported cathode materials in organic electrolytes (Fig. 4e). Among the reported cathode materials, 3D rGO aerogel, NHVO, and NVO all exhibit the longest cycle life and high-capacity retention. In particular, NVO exhibits an ultra-long life of 60 000 cycles (more than 600 days) and a capacity retention of 75%, which further suggests that high-solvation $Ca(TFSI)_2$-based electrolytes may be the best choice for ultra-stable calcium-ion storage.

A Ca-ion full cell (NVO‖$Ca_xTi_3C_2$) with the $Ca(TFSI)_2$/G4 electrolyte was assembled. The NVO‖$Ca_xTi_3C_2$ full cell has a discharge capacity of 69.1 mA h g^{-1} (Fig. S28a, ESI†) and 60 cycles life at 20 mA g^{-1} and room temperature (Fig. S28b, ESI†), which indicates that the potential application of NVO cathode materials and $Ca(TFSI)_2$/G4 electrolyte in CIBs. To further

underscore the potential of NVO in Ca–metal batteries, a NVO‖$Ca[B(hfip)_4]_2$/DME‖Ca battery was assembled and exhibits a 174.7 mA h g^{-1} discharge capacity (Fig. S29a, ESI†), affirming the viability of NVO in Ca–metal batteries. However, after 10 cycles, the capacity dwindled to 50.7 mA h g^{-1} (Fig. S29b, ESI†). This decline is attributed to the insufficient compatibility between $Ca[B(hfip)_4]_2$/DME and the Ca–metal anode.[48] Therefore, enhancing the compatibility between the electrolyte and the Ca metal is pivotal for advancing CIBs, and it will be a primary focus of our forthcoming endeavors. Moreover, in the Ca-system without using a Ca metal anode, a graphite anode with the low working voltage may be a suitable option to enhance the working voltage of Ca-ion full cells.[49] However, the low specific capacity of the graphite anode limits its commercial application. Therefore, it is also crucial to further improve the CE and specific capacity of the graphite anode through the electrolyte solvation structure regulation or material modification in the future work.

Storage and activation mechanism in high-solvation electrolytes

In situ XRD was used to investigate the Ca^{2+} storage mechanism of NVO. In $Ca(TFSI)_2$/G4, the (001) diffraction peak of NVO shifts to high angle during the discharge process, indicating that the interlayer spacing of NVO decreases (Fig. 5a). Meanwhile, the (−301), (110) and (−211) diffraction peaks of NVO shift to low angle, meaning the increase of *a* and *b*. During the charge process, all the diffraction peaks shift reversely and return to the initial position at the end, which indicates that NVO has good structural reversibility and the calcium storage

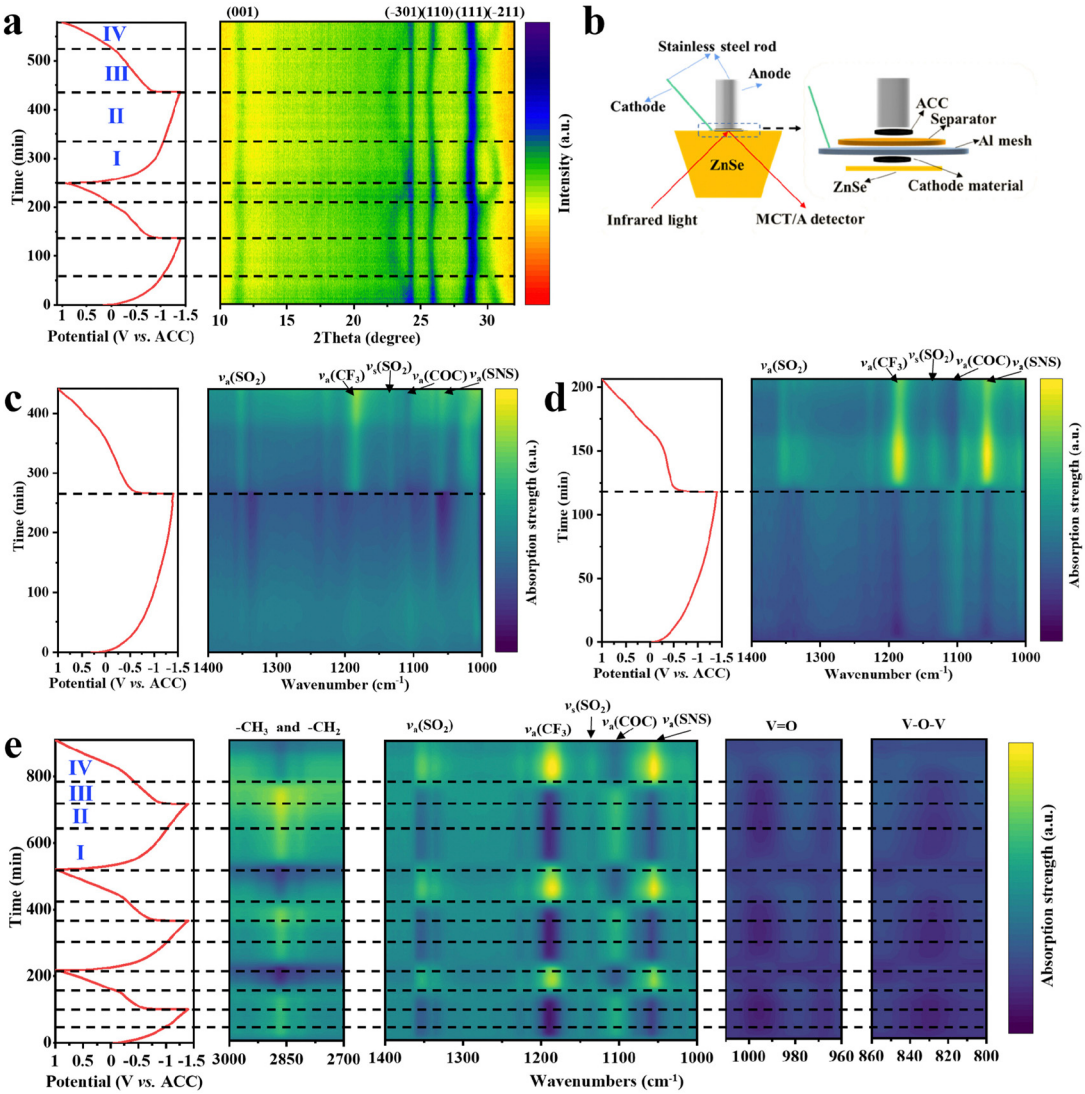

Fig. 5 Calcium storage mechanisms of NVO in high-solvation electrolytes. (a) *In situ* XRD patterns of NVO and the corresponding charge/discharge profiles in the $Ca(TFSI)_2$/G4 electrolyte. (b) The configuration of the cell for *in situ* ATR-FTIR tests. (c)–(e) *In situ* ATR-FTIR spectra of NVO and the corresponding charge/discharge curves in (c) $Ca(TFSI)_2$/DME, (d) $Ca(TFSI)_2$/G2 and (e) $Ca(TFSI)_2$/G4 electrolytes. All *in situ* tests were performed at room temperature.

mechanism of NVO is a single-phase solid solution reaction in the $Ca(TFSI)_2$/G4 electrolyte. Interestingly, the shift of the diffraction peaks is not monotonic in the $Ca(TFSI)_2$/G4 electrolyte. In stage I, the (111) and (−211) diffraction peaks shift significantly, while the (−301) and (110) diffraction peaks shift slightly. In stage II, the (111) and (−211) diffraction peaks shift slightly, and the (−301) and (110) diffraction peaks shift significantly. During the charge process, two similar stages are observed. However, the changes of these diffraction peaks in the $Ca(TFSI)_2$/G2 electrolyte are different (Fig. S30, ESI†), which may be due to the presence of solvation co-insertion in high-solvation $Ca(TFSI)_2$/G4 electrolyte. The research on solvation co-insertion will be further discussed later.

The dynamic behaviors of electrolytes on NVO electrodes were studied by *in situ* ATR-FTIR spectroscopy. The configuration of the cell for *in situ* ATR-FTIR tests is shown in Fig. 5b, and the FTIR spectra of different solvents and electrolytes are shown in Fig. S31 (ESI†). *In situ* ATR-FTIR spectra of NVO in $Ca(TFSI)_2$/DME (Fig. 5c) indicate that the intensity of the corresponding $TFSI^-$ absorption peaks (including $\nu_a(SO_2)$, $\nu_a(CF_3)$, $\nu_s(SO_2)$ and $\nu_a(SNS)$) gradually weakens[50,51] and the intensity of the corresponding DME solvent absorption peak ($\nu_a(COC)$)[52] increases during discharge, which is due to the migration of $TFSI^-$ to the anode and the desolvation of Ca^{2+} at the interface of the cathode. The reverse peak evolution is observed during charge. In $Ca(TFSI)_2$/G2, similar changes of the absorption peaks were observed, and the more pronounced intensity change is due to the stronger interaction between G2 and Ca^{2+} (Fig. 5d). In $Ca(TFSI)_2$/G4, the observed absorption peak changes are different from that of other two electrolytes (Fig. 5e). Two distinct stages are observed during discharge and charge, respectively, which are similar to the changes in the *in situ* XRD pattern (Fig. 5a). It is particularly noteworthy that the intensity of the corresponding G4 solvent absorption peaks, including C–O–C, $-CH_3$ and $-CH_2$, remain unchanged at stage III, which may be caused by G4 solvent co-extraction during charge, corresponding to the presence of solvent co-insertion during discharge. However, *in situ* ATR-FTIR spectra of NVO for the high wavenumber regions (Fig. S32, ESI†) indicate that there is no solvent co-insertion phenomenon in $Ca(TFSI)_2$/DME and $Ca(TFSI)_2$/G2 electrolytes. In addition, *in situ* ATR-FTIR spectra reveal the reversible shifts of V═O and V–O–V absorption bands, further demonstrating the good structural reversibility of NVO. 1D *in situ* ATR-FTIR spectra of NVO for all 2D plots are additionally shown in Fig. S33–S35 (ESI†).

Ex situ FTIR, inductively coupled plasma atomic emission spectroscopy (ICP-AES), TEM and 3D visualization of tomographic reconstruction techniques were performed to reveal the solvent co-insertion phenomenon and the activation process mechanism during the initial cycles. The *ex situ* FTIR spectra of G4 solvent and NVO in $Ca(TFSI)_2$/G4 electrolyte show that the absorption peak of G4 is absent at −0.8 V and appears at −1.4 V (Fig. 6a), indicating the solvent co-insertion at low potential. The reversible process can be observed during the charge. The results further confirm the existence of two distinct stages during discharge or charge and solvent co-insertion, consistent with the *in situ* XRD and *in situ* ATR-FTIR results. However, the FTIR spectra of the discharged NVO in $Ca(TFSI)_2$/DME and $Ca(TFSI)_2$/G2 have no absorption peaks of solvents (Fig. 6b).

The ICP-AES data of NVO electrodes at different states after different cycles (Fig. 6c) indicate that the amount of Ca^{2+} ions in NVO increases and a small amount of Na is de-inserted from NVO during the cycling process. At the 10th cycle, the molar ratio of Ca : V is 0.45, corresponding to a capacity of 217 mA h g^{-1}, which is close to the discharge capacity of NVO (Fig. 4a). The ICP-AES data show that the increase in specific capacity is due to the increase in the amount of inserted Ca^{2+}, so the reason why the inserted Ca^{2+} ions increase during cycling needs to be further revealed. The high spatial and energy resolution of electron energy-loss spectroscopy (EELS) mappings were used to analyze the distribution of Ca in NVO in different states. The ADF image of the discharged NVO and the corresponding EELS mappings of V and Ca (Fig. 6d), at the 1st cycle, reveal that element Ca accumulates at the ends of the nanowires, meaning that Ca^{2+} ions are inserted into nanowires from the ends. At the 10th cycle, the element Ca is evenly distributed in nanowires (Fig. 6e), further confirming the increase in the amount of inserted Ca^{2+} and the presence of an activation process. The 3D reconstruction and orthoslicing images of NVO nanowires (Fig. 6f–h and Fig. S36–S38, ESI†) after the first 10 cycles demonstrate that there are some voids (black circles) inside NVO nanowires and some nanowires are broken (yellow circles), which will increase the contact area between NVO and electrolyte. In addition, Ca^{2+} may be inserted from the end of nanowires, and broken nanowires are beneficial to increase the Ca^{2+} storage activity of NVO. The electrochemical impedance spectra (EIS) of NVO at different cycles (Fig. S39, ESI†) show a decrease in interfacial charge transfer resistance with cycling, which is also conducive to the insertion of Ca^{2+} ions. The rotational and orthogonal slicing processes are shown in Movies S1 and S2 (ESI†). *Ex situ* TEM images with different magnifications after 10 cycles also show that some NVO nanowires are broken (Fig. S40, ESI†). The above results suggest that the activation process is due to the fracture of NVO nanowires. The effect of NVO nanowires fracture on solvents insertion is studied. The EDX spectra of NVO with different states (initial state, 2nd discharged state, and 5th discharged state) indicate a gradual decrease in the atomic ratio of V to O (Fig. S41, ESI†), implying an increase in solvents insertion.[49]

The insertion/extraction and storage sites of Ca^{2+} were further investigated by *ex situ* XPS, density functional theory (DFT) computations, and atomic-resolution TEM. The *ex situ* Ca 2p XPS spectra of NVO (Fig. 6i) indicate that two strong peaks corresponding to the Ca 2p signal are observed for discharged NVO and the peak intensity of Ca 2p becomes weak for charged NVO, demonstrating the insertion/extraction of Ca^{2+} during discharge/charge. Some other characterizations, to prove the insertion of Ca^{2+} and the change of vanadium valence, are shown in Fig. S42–S46 (ESI†), including *ex situ* XPS, EELS, and TEM. Additionally, the vanadium K-edge X-ray absorption near-edge spectra (XANES) spectra of NVO at the initial state and

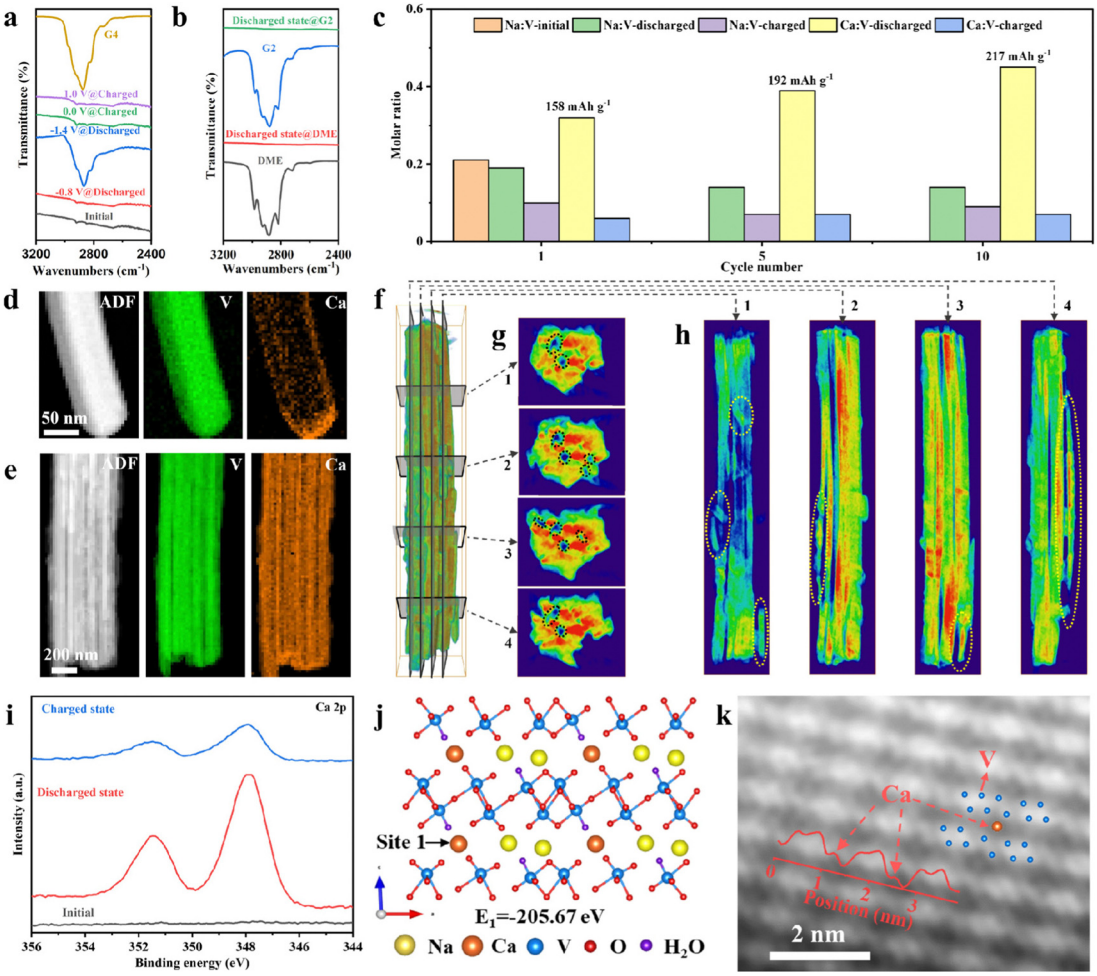

Fig. 6 Characterization of solvent co-insertion, the activation mechanisms, and the storage sites of Ca^{2+} in high-solvation electrolytes. (a) FTIR spectra of G4 solvent and different states NVO in $Ca(TFSI)_2$/G4 electrolyte. (b) FTIR spectra of DME, G2 solvents, discharged NVO in $Ca(TFSI)_2$/DME and $Ca(TFSI)_2$/G2 electrolytes. (c) ICP-AES data of NVO with different states and cycles in $Ca(TFSI)_2$/G4 electrolyte. (d) and (e) ADF image of the fully discharged NVO and EELS mappings of V, Ca at (d) the first cycle and (e) the 10th cycle with $Ca(TFSI)_2$/G4 electrolyte. (f)–(h) 3D visualization of tomographic reconstruction images of NVO after first 10 cycles in $Ca(TFSI)_2$/G4 electrolyte. (i) *Ex situ* XPS spectra of Ca 2p for NVO at different states. (j) The Ca^{2+} storage sites (site 1) of NVO determined by DFT calculation. (k) HAADF-STEM images of fully discharged NVO and the inset is the intensity profiles for the corresponding position.

fully discharged state show that the K-edge of the vanadium of the fully discharged NVO shifts to low energy (Fig. S47a, ESI†), indicating that V^{5+} is reduced during discharge. The corresponding Fourier transform extended X-ray absorption fine structure (FT-EXAFS) spectra in *R* space indicate the V–O distance of initial NVO are 1.06 Å and 1.57 Å (Fig. S47b, ESI†), and the change of the bond length can be observed for the fully discharged NVO, which is due to the insertion of Ca^{2+} during discharge. DFT computation results show that there are two possible Ca^{2+} storage sites in NVO (named site 1 and site 2, Fig. 6j and Fig. S48, ESI†) and Ca^{2+} ions prefer to occupy site 1 to form a more thermodynamically stable structure with a lower formation energy of −205.67 eV (Fig. 6j). Double spherical aberration correction TEM was further used to study the insertion sites of Ca^{2+} ions. The HAADF-STEM images of fully discharged NVO and the intensity profiles for the corresponding position (Fig. 6k) confirm that Ca^{2+} ions are inserted into site 1, which is consistent with DFT calculations. The Ca^{2+} storage site of NVO is determined for the first time at the atomic scale. The feasibility of site 1 accommodating solvent co-insertion is further investigated through DFT calculations. The spatial size of site 1, shown in Fig. S49 (ESI†), indicates that one Ca^{2+} ion and one G4 molecule can be placed into site 1. After relaxation, the NVO structure with co-inserted Ca^{2+} ions and G4 solvent can exist stably (Fig. S50, ESI†). These results suggest that G4 solvent co-insertion into site 1 is theoretically possible. However, the extent of solvent insertion may require further experimental and theoretical studies.

Conclusions

In summary, we found that the decomposition of $TFSI^-$ ions and the formation of the CaF_2-rich CEI can be suppressed in a

high-solvation $Ca(TFSI)_2$/G4 electrolyte, which can effectively alleviate the depletion of electrolyte and the irreversible capacity loss, endowing CIBs with excellent stability. With the high-solvation $Ca(TFSI)_2$/G4 electrolyte, NVO as a cathode material for CIBs exhibits a high discharge capacity of 240.7 mA h g^{-1}, an ultra-long life of 20 000 cycles at room temperature and 60 000 cycles (over 600 days) at 50 °C. In addition, the high-solvation $Ca(TFSI)_2$/G4 electrolyte has good compatibility with other electrode materials. The phenomenon of co-insertion of solvents into the high-solvation $Ca(TFSI)_2$/G4 electrolyte is revealed by *in situ* ATR-FTIR and *ex situ* FTIR. *In situ* XRD and *ex situ* TEM results show that the calcium storage mechanism of NVO is a single-phase solid solution reaction. The crystal structure of NVO and the Ca^{2+} storage site of NVO were determined for the first time at the atomic scale by double aberration correction TEM. These findings provide a $Ca(TFSI)_2$-based electrolyte design principle by adjusting the solvent chemistry to enable the electrode materials for CIBs with ultra-long life and are expected to encourage more research to promote the development of CIBs.

Experimental section

Experimental details and characterization are included in the ESI.†

Author contributions

L. M., Q. A. and G. H. proposed and supervised the research. J. W. designed the experimental method, performed electrochemical testing and data analysis, and wrote the first draft. F. Q. and J. W. performed material preparation and characterization. R. Y. performed characterization and analysis related to transmission electron microscopy. X. L. performed force-field based classical molecular dynamics simulations. Y. J. performed density functional theory calculations. M. H., F. X., L. C., Y. D., L. Z., G. H., Q. A., and L. M. contributed to the revision of the manuscript.

Data availability

The data that support the findings of this study are included in the published article and its ESI.† These data are also available from the corresponding authors upon request.

Conflicts of interest

There are no conflicts to declare.

Acknowledgements

This work was supported by the National Natural Science Foundation of China (52172231, 52127816, and 52202290), the National Key Research and Development Program of China (2020YFA0715000), the Engineering and Physical Sciences Research Council (EPSRC, EP/V027433/3), UK Research and Innovation (UKRI) under the UK government's Horizon Europe funding (101077226; EP/Y008707/1), the Natural Science Foundation of Hubei Province (2022CFA087, and 2022CFD090) and the Sanya Science and Education Innovation Park of Wuhan University of Technology (2022KF0011). Junjun Wang is grateful for the funding support from China Scholarship Council/University College London for the joint PhD scholarship (CXXM2110070005). The project is supported by the State Key Laboratory of Advanced Technology for Materials Synthesis and Processing (Wuhan University of Technology).

References

1 M. E. Arroyo-de Dompablo, A. Ponrouch, P. Johansson and M. R. Palacin, *Chem. Rev.*, 2020, **120**, 6331–6357.
2 M. Wang, C. Jiang, S. Zhang, X. Song, Y. Tang and H. M. Cheng, *Nat. Chem.*, 2018, **10**, 667–672.
3 S. Hou, X. Ji, K. Gaskell, P. F. Wang, L. Wang, J. Xu, R. Sun, O. Borodin and C. Wang, *Science*, 2021, **374**, 172–178.
4 S. D. Pu, C. Gong, X. Gao, Z. Ning, S. Yang, J.-J. Marie, B. Liu, R. A. House, G. O. Hartley, J. Luo, P. G. Bruce and A. W. Robertson, *ACS Energy Lett.*, 2020, **5**, 2283–2290.
5 A. Ponrouch, C. Frontera, F. Barde and M. R. Palacin, *Nat. Mater.*, 2016, **15**, 169–172.
6 D. Wang, X. Gao, Y. Chen, L. Jin, C. Kuss and P. G. Bruce, *Nat. Mater.*, 2018, **17**, 16–20.
7 Z. Li, O. Fuhr, M. Fichtner and Z. Zhao-Karger, *Energy Environ. Sci.*, 2019, **12**, 3496–3501.
8 Z. Hou, R. Zhou, Y. Yao, Z. Min, Z. Lu, Y. Zhu, J. M. Tarascon and B. Zhang, *Angew. Chem., Int. Ed.*, 2022, **61**, e202214796.
9 Y. Jin, P. M. L. Le, P. Gao, Y. Xu, B. Xiao, M. H. Engelhard, X. Cao, T. D. Vo, J. Hu, L. Zhong, B. E. Matthews, R. Yi, C. Wang, X. Li, J. Liu and J.-G. Zhang, *Nat. Energy*, 2022, **7**, 718–725.
10 P. Bai, X. Ji, J. Zhang, W. Zhang, S. Hou, H. Su, M. Li, T. Deng, L. Cao, S. Liu, X. He, Y. Xu and C. Wang, *Angew. Chem., Int. Ed.*, 2022, **61**, e202202731.
11 J. Li, Y. Hu, H. Xie, J. Peng, L. Fan, J. Zhou and B. Lu, *Angew. Chem., Int. Ed.*, 2022, **61**, e202208291.
12 Q. Ma, R. Gao, Y. Liu, H. Dou, Y. Zheng, T. Or, L. Yang, Q. Li, Q. Cu, R. Feng, Z. Zhang, Y. Nie, B. Ren, D. Luo, X. Wang, A. Yu and Z. Chen, *Adv. Mater.*, 2022, **34**, 2207344.
13 J. Forero-Saboya, C. Davoisne, R. Dedryvère, I. Yousef, P. Canepa and A. Ponrouch, *Energy Environ. Sci.*, 2020, **13**, 3423–3431.
14 N. T. Hahn, D. M. Driscoll, Z. Yu, G. E. Sterbinsky, L. Cheng, M. Balasubramanian and K. R. Zavadil, *ACS Appl. Energy Mater.*, 2020, **3**, 8437–8447.
15 D. M. Seo, O. Borodin, S.-D. Han, P. D. Boyle and W. A. Henderson, *J. Electrochem. Soc.*, 2012, **159**, A1489–A1500.
16 A. Bakker, J. Lindgren and K. Hermansson, *Polymer*, 1996, **37**, 1871–1878.
17 Y. Zhang, G. Wan, N. H. C. Lewis, J. Mars, S. E. Bone, H.-G. Steinrück, M. R. Lukatskaya, N. J. Weadock, M. Bajdich,

O. Borodin, A. Tokmakoff, M. F. Toney and E. J. Maginn, *ACS Energy Lett.*, 2021, **6**, 3458–3463.
18 N. H. C. Lewis, Y. Zhang, B. Dereka, E. V. Carino, E. J. Maginn and A. Tokmakoff, *J. Phys. Chem. C*, 2020, **124**, 3470–3481.
19 X. Liu, G. A. Elia and S. Passerini, *J. Power Sources Adv.*, 2020, **2**, 100008.
20 M. S. Chae, H. H. Kwak and S.-T. Hong, *ACS Appl. Energy Mater.*, 2020, **3**, 5107–5112.
21 M. S. Chae, A. Nimkar, N. Shpigel, Y. Gofer and D. Aurbach, *ACS Energy Lett.*, 2021, **6**, 2659–2665.
22 S. Kim, L. Yin, M. H. Lee, P. Parajuli, L. Blanc, T. T. Fister, H. Park, B. J. Kwon, B. J. Ingram, P. Zapol, R. F. Klie, K. Kang, L. F. Nazar, S. H. Lapidus and J. T. Vaughey, *ACS Energy Lett.*, 2020, **5**, 3203–3211.
23 R. Zhou, Z. Hou, Q. Liu, X. Du, J. Huang and B. Zhang, *Adv. Funct. Mater.*, 2022, **32**, 2200929.
24 J. Wang, J. Wang, Y. Jiang, F. Xiong, S. Tan, F. Qiao, J. Chen, Q. An and L. Mai, *Adv. Funct. Mater.*, 2022, **32**, 2113030.
25 C. Zuo, F. Xiong, J. Wang, Y. An, L. Zhang and Q. An, *Adv. Funct. Mater.*, 2022, **32**, 2202975.
26 J. Wang, S. Tan, F. Xiong, R. Yu, P. Wu, L. Cui and Q. An, *Chem. Commun.*, 2020, **56**, 3805–3808.
27 M. Cabello, F. Nacimiento, R. Alcántara, P. Lavela, C. Pérez Vicente and J. L. Tirado, *Chem. Mater.*, 2018, **30**, 5853–5861.
28 B. Jeon, H. H. Kwak and S.-T. Hong, *Chem. Mater.*, 2022, **34**, 1491–1498.
29 D. S. Tchitchekova, A. Ponrouch, R. Verrelli, T. Broux, C. Frontera, A. Sorrentino, F. Bardé, N. Biskup, M. E. Arroyo-de Dompablo and M. R. Palacín, *Chem. Mater.*, 2018, **30**, 847–856.
30 J. Hyoung, J. W. Heo, B. Jeon and S.-T. Hong, *J. Mater. Chem. A*, 2021, **9**, 20776–20782.
31 T. N. Vo, H. Kim, J. Hur, W. Choi and I. T. Kim, *J. Mater. Chem.*, 2018, **6**, 22645–22654.
32 P. Padigi, G. Goncher, D. Evans and R. Solanki, *J. Power Sources*, 2015, **273**, 460–464.
33 R. Verrelli, A. Black, R. Dugas, D. Tchitchekova, A. Ponrouch and M. R. Palacin, *J. Electrochem. Soc.*, 2020, **167**, 070532.
34 Z. L. Xu, J. Park, J. Wang, H. Moon, G. Yoon, J. Lim, Y. J. Ko, S. P. Cho, S. Y. Lee and K. Kang, *Nat. Commun.*, 2021, **12**, 3369.
35 C. Chen, F. Shi, S. Zhang, Y. Su and Z. L. Xu, *Small*, 2022, **18**, e2107853.
36 X. Zhang, X. Xu, B. Song, M. Duan, J. Meng, X. Wang, Z. Xiao, L. Xu and L. Mai, *Small*, 2022, **18**, e2107174.
37 Z. Li, B. P. Vinayan, P. Jankowski, C. Njel, A. Roy, T. Vegge, J. Maibach, J. M. G. Lastra, M. Fichtner and Z. Zhao-Karger, *Angew. Chem., Int. Ed.*, 2020, **59**, 11483–11490.
38 J. Bitenc, A. Scafuri, K. Pirnat, M. Lozinsek, I. Jerman, J. Grdadolnik, B. Fraisse, R. Berthelot, L. Stievano and R. Dominko, *Batteries Supercaps*, 2021, **4**, 214–220.
39 S. Zhang, Y. Zhu, D. Wang, C. Li, Y. Han, Z. Shi and S. Feng, *Adv. Sci.*, 2022, **9**, e2200397.
40 Z. Zhao-Karger, Y. Xiu, Z. Li, A. Reupert, T. Smok and M. Fichtner, *Nat. Commun.*, 2022, **13**, 3849.
41 A. L. Lipson, B. Pan, S. H. Lapidus, C. Liao, J. T. Vaughey and B. J. Ingram, *Chem. Mater.*, 2015, **27**, 8442–8447.
42 A. L. Lipson, S. Kim, B. Pan, C. Liao, T. T. Fister and B. J. Ingram, *J. Power Sources*, 2017, **369**, 133–137.
43 N. Kuperman, P. Padigi, G. Goncher, D. Evans, J. Thiebes and R. Solanki, *J. Power Sources*, 2017, **342**, 414–418.
44 M. E. Purbarani, J. Hyoung and S.-T. Hong, *ACS Appl. Energy Mater.*, 2021, **4**, 7487–7491.
45 S. J. R. Prabakar, W.-B. Park, J. Y. Seo, S. P. Singh, D. Ahn, K.-S. Sohn and M. Pyo, *Energy Storage Mater.*, 2021, **43**, 85–96.
46 Z. Hou, R. Zhou, Z. W. Min, Z. H. Lu and B. Zhang, *ACS Energy Lett.*, 2022, **8**, 274–279.
47 D. M. Driscoll, N. K. Dandu, N. T. Hahn, T. J. Seguin, K. A. Persson, K. R. Zavadil, L. A. Curtiss and M. Balasubramanian, *J. Electrochem. Soc.*, 2020, **167**, 160512.
48 K. V. Nielson, J. Luo and T. L. Liu, *Batteries Supercaps*, 2020, **3**, 766–772.
49 S. J. Richard Prabakar, A. B. Ikhe, W. B. Park, K. C. Chung, H. Park, K. J. Kim, D. Ahn, J. S. Kwak, K. S. Sohn and M. Pyo, *Adv. Sci.*, 2019, **6**, 1902129.
50 A. G. Bishop, D. R. MacFarlane, D. McNaughton and M. Forsyth, *J. Phys. Chem.*, 1996, **100**, 2237–2243.
51 M. Chiku, S. Matsumura, H. Takeda, E. Higuchi and H. Inoue, *J. Electrochem. Soc.*, 2017, **164**, A1841–A1844.
52 F. Shi, P. N. Ross, H. Zhao, G. Liu, G. A. Somorjai and K. Komvopoulos, *J. Am. Chem. Soc.*, 2015, **137**, 3181–3184.

